Journal of Alloys and Compounds 498 (2010) 81–87

Contents lists available at ScienceDirect

Journal of Alloys and Compounds

journal homepage: www.elsevier.com/locate/jallcom

Preparation and optical properties of Eu^{3+}-doped tin oxide nanoparticles

Guofeng Wang, Yiping Yang, Qiuying Mu, Yude Wang*

Department of Materials Science and Engineering, Yunnan University, Kunming 650091, PR China

ARTICLE INFO

Article history:
Received 2 February 2010
Received in revised form 9 March 2010
Accepted 9 March 2010
Available online 17 March 2010

Keywords:
Eu^{3+}-doped SnO_2
Nanoparticles
Surfactant-mediated method
Room temperature photoluminescence

ABSTRACT

Eu^{3+}-doped SnO_2 nanoparticles with high surface area were generated within the template of the cationic surfactant (cetyltrimethylammonium bromide, CTAB) micelle assembly by surfactant-mediated method from the hydrous tin chloride ($SnCl_4{\cdot}5H_2O$) and europium chloride ($EuCl_3{\cdot}6H_2O$). The as-synthesized product was amorphous and transformed into crystalline calcined at 500 °C for 2 h. DSC-TGA, X-ray powder diffraction (XRD), transmission electron microscopy (TEM), and X-ray photoelectron spectroscopy (XPS) were used to examine the morphology and microstructure of the final products. The results showed that the Eu^{3+}-doped SnO_2 nanoparticles with diameter of 3–7 nm were obtained. The influences of the molar ratios of Eu^{3+} and CTAB on the room temperature photoluminescence (RTPL) properties of Eu^{3+}-doped SnO_2 nanoparticles were investigated. The results showed that the contents of Eu^{3+} and CTAB had a great influence on the crystallite sizes and RTPL properties of Eu^{3+}:SnO_2 nanoparticles. The maximum of the RTPL intensity can be observed at the molar ratio 5.0% Eu^{3+} and 10.0% CTAB.

1. Introduction

Tin oxide is an n-type semiconductor oxide with a wide-energy-gap (E_g = 3.62 eV, at 300 K). It is particularly interesting because it has semiconducting properties and has been widely used as a catalyst for oxidation of organic compounds, and as gas sensors [1,2], rechargeable Li-batteries, and optical electronic devices [3]. It is a very important technology for the doping to control the behavior of materials. Many researchers have begun to explore the dopants influences on semiconductor nanocrystals and the unusual and size-specific optical and electronic behaviors [4,5]. Recently, considerable research has been focused on rare-earth (RE) ion doped semiconductors for novel properties, especially the photoluminescent properties [6–11]. The band gap excitation may result in efficient energy transfer and hence intense luminescence from the rare-earth ion. The optical property of doped semiconductor nanoparticles has given rise to intriguing science in nanoresearch in the new millennium. According to its unique fluorescent properties, stability, and high emission-quantum yield, the Eu^{3+} ion as an activator has been investigated much frequently. Eu^{3+}-doped SnO_2 nanoparticle is a typical material, which has been widely studied. It was found the Eu^{3+} emission is strongly enhanced by energy transfer from the SnO_2 nanocrystals in a glass matrix [12,13]. Recently, it was reported that Eu^{3+}-activated SnO_2 nanocrystals showed good luminescence properties [11,14–17]. It was found that the spontaneous emission probability of optical transitions from rare-earth ions doped in nanoparticles could be significantly modified by contents of Eu^{3+}, changing the particle size, shape, and surrounding medium.

Owing to such a large range of applications, various methods have been applied for the synthesis of tin oxide nanoparticles. For Eu^{3+}-doped SnO_2 nanoparticles, it is difficult for Eu^{3+} ions to enter the lattice of SnO_2 because of the large difference of the radius and charge between Eu^{3+} and Sn^{4+} [18]. It results in the poor luminescence of the phosphor. A variety of techniques has been usually used to synthesize oxides nanoparticles including hydrothermal, coprecipitation, combustion, sol–gel, solvothermal, and microemulsions routes [19–25]. However, these methods are the challenge to prepare SnO_2 powders with particle size about several nanometers, and require very stringent control in various processing parameters, together with a low production yield. Therefore, it is necessary to find a new method for preparing Eu^{3+}:SnO_2 nanoparticles. Herein, we report the room temperature photoluminescence (RTPL) properties of Eu^{3+}:SnO_2 nanoparticles prepared using a simple surfactant-mediated method. The method is based on the cationic surfactant cetyltrimethylammonium bromide (CTAB) and simple chemical reagents (hydrous metal chloride ($SnCl_4{\cdot}5H_2O$), europium chloride ($EuCl_3{\cdot}6H_2O$), and $NH_3{\cdot}H_2O$). The cations (Sn and Eu) are assembled within the template of surfactant micelle in an aqueous solution. The surfactant not only provides a favorable site for the growth of the particulate assemblies, but also influences the formation process, including nucleation, growth, coagulation and flocculation [26]. Surfactant and Eu^{3+} play an important role in the preparation and the optical properties of Eu^{3+}:SnO_2 nanoparticles. Eu^{3+}-doped SnO_2 nanoparticles with a mean particle diameter of 3–7 nm have

* Corresponding author. Fax: +86-871-5035376.
E-mail address: ydwang@ynu.edu.cn (Y. Wang).

0925-8388/$ – see front matter © 2010 Elsevier B.V. All rights reserved.
doi:10.1016/j.jallcom.2010.03.107

been successfully prepared. The properties of the materials were characterized by X-ray diffraction (XRD) analysis, thermogravimetric analysis (TGA), transmission electron microscopy (TEM), X-ray photoelectron spectroscopy (XPS), and room temperature photoluminescence (RTPL) experiments.

2. Experimental

2.1. Preparation of Eu^{3+}-doped SnO_2 nanoparticles

All the chemical reagents used in the experiments were obtained from commercial sources as guaranteed-grade reagents and used without further purification. The purity of CTAB was 99% and the inorganic precursors were not less than 99%, respectively. The synthesized method was based on the use of the cationic surfactant (CTAB) and the simple chemical materials (hydrous tin chloride, europium chloride, and $NH_3{\cdot}H_2O$) as inorganic precursors at room temperature. In a typical process, the synthetic procedures were as follows: the CTAB was mixed with distilled deionized water with stirring until a homogenous solution (0.08 M) was obtained. The solution of diluted $NH_3{\cdot}H_2O$ (25 wt.% solution, 10 ml) was then added into the CTAB solution with stirring. The initial solutions were prepared by dissolving 350 mg $SnCl_4{\cdot}5H_2O$ and 5.0% molar ratio Eu^{3+} in 10 mL distilled deionized water. When the mixing solution became homogenous, the solution of $SnCl_4$ and $EuCl_3$ was added, respectively, under vigorous stirring. After stirring 4 h, the products were aged at ambient temperature for 96 h. The resulting product was filtered, washed with distilled water to remove surfactant, and then dried at ambient temperature. Complete evolution of the surfactant from the as-synthesized product to yield the tin oxide nanoparticles was achieved through thermal treatment at 250 °C with a ramp of 1 °C/min for 2 h and at 500 °C for 2 h with a ramp of 2 °C/min under flowing air atmosphere. Eu^{3+}:SnO_2 samples with the different molar ratios Eu^{3+} (0, 2.5, 5.0, 7.5, and 10.0%) and the different molar ratios CTAB (Sn:CTAB = 2.5, 5.0, 7.5, 10.0, and 12.5%) were studied, respectively.

2.2. Characterization of Eu^{3+}-doped SnO_2 nanoparticles

Thermogravimetric analysis (TGA and DSC) curves were obtained in flowing air on NETZSCH STA 409 PG/PC with a temperature increasing rate of 10 °C/min. X-ray diffraction (XRD, Rigaku D/MAX-3B powder diffractometer) with copper target and Kα radiation (λ = 1.54056 Å) was used for the phase identification, where the diffracted X-ray intensities were recorded as a function of 2θ. The sample was scanned from 20° to 80° (2θ) in steps of 0.02°. The crystallite domain sizes (D) have been examined from XRD peaks based on the Scherrer's equation: $D = 0.9\lambda/(\Delta W \cos\theta)$, where λ is the wavelength of X-ray, θ is the Bragg's diffraction angle, and ΔW is the true half-peak width of the X-ray diffraction lines. The transmission electron micrographs (TEM) were made with on a Zeiss EM 912 Ω instrument at an acceleration voltage of 120 kV. The samples for TEM were prepared by dispersing the final powders in ethanol; this dispersing was then dropped on carbon–copper grids. X-ray photoelectron spectroscopy (XPS) was carried out at room temperature in ESCALAB 250 system. During XPS analysis, an Al Kα X-ray beam was adopted as the excitation source and the vacuum pressure of the instrument chamber was 1×10^{-7} Pa. UV/Vis measurements were made with a UV-2401PC spectrophotometer. Photoluminescence (PL) experiments were measured on a Hitachi F-4500 FL Spectrophotometer using a xenon lamp as the excitation source at room temperature. All experiments were performed at room temperature. The sample was dispersed in dichloromethane and the excitation wavelength used in PL measurement was 395 nm.

2.3. Detail of the simulating XRD powder pattern

The recorded XRD powder patterns were processed with the Rietveld method using the program FULLPROF. The details were performed as previously reported [27,28].

3. Results and discussion

Thermogravimetric analysis (TGA) of the as-synthesized sample (with 5.0% molar ratio Eu^{3+}) under air shows three apparent decreases in specimen weight (Fig. 1). The first is over the temperature range from room temperature to *ca.* 170 °C, the second is over the temperature range from 170 to *ca.* 300 °C, and the third is from 300 to 500 °C. The loss of water is below 170 °C and of the surfactant starts at 170 °C. At about 500 °C, the surfactant is completely removed. The analysis of the as-synthesized sample reveals ~39% total weight loss on heating to 500 °C. Presumably, the first effect is attributed to the release of residual solvent and adsorbed water, the second to desorption and decomposition of the surfactant template, and the third to dehydroxylation of the surface and removal

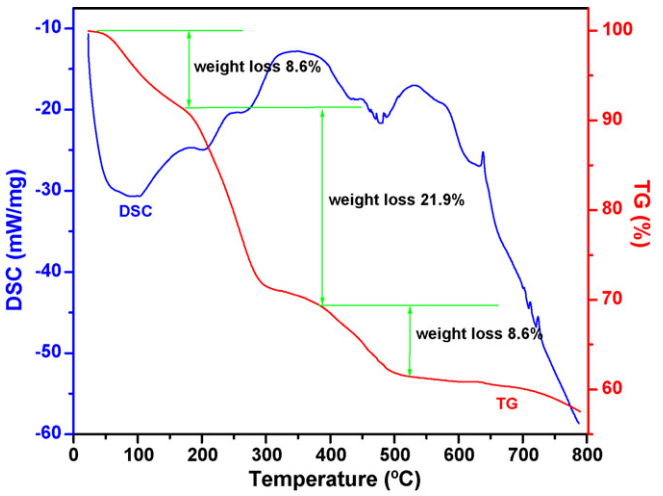

Fig. 1. DSC and TGA curves of as-synthesized sample (with 5.0% molar ratio Eu^{3+}).

of little residual surfactant [29–31]. No weight loss can be observed at above 500 °C, indicating the completion of any reaction involving a weight change. From these results, it is clear that most of the surfactant CTAB in the as-synthesized powder is eliminated at about 500 °C. The same results can be found for the other samples. The organic CTAB can be completely removed in the calcination step because a low heating rate was used in the preparation. (TGA measurements were performed with 10 °C/min, in contrast to only 1 °C/min and 2 °C/min heating in the calcination program. In addition, it contained 2 h holding steps at 250 °C and 500 °C.) Therefore, the calcining of the sample in air has been performed at 500 °C.

Fig. 2 shows the X-ray diffraction patterns of the samples, which are prepared with different molar ratios Eu^{3+} (Eu^{3+}:Sn = 0, 2.5, 5.0, 7.5, and 10.0%) and different molar ratios CTAB (CTAB:Sn = 2.5, 5.0, 7.5, 10.0, and 12.5%) after the final heat treatment at 500 °C for 2 h, respectively. The effects of the different molar ratios of Eu^{3+} and CTAB on the crystallographic structure for samples did not reveal from Fig. 2. The XRD patterns revealed well-developed reflections of cassiterite SnO_2 (ICDD PDF No. 41-1445), without any indications of the by-products such as Eu_2O_3 or $Eu_2Sn_2O_7$. This finding implies that the europium doping most probably occurs by substituting tin atoms in the crystal structure. The mean grain size (D) of the Eu^{3+}-doped SnO_2 nanoparticles was calculated by using the Scherrer equation to the (1 1 0) plane diffraction peak (2θ = 26.6°). The crystalline grain sizes of Eu^{3+}-doped SnO_2 nanoparticles decreased from 6.7 to 3.6 nm when the Eu^{3+} content increased from 0.0 to 10%. The Eu-doping makes effects on the size of the nanoparticles. Fig. 2(a) showed a decrease of crystallinity in the Eu^{3+}-doped SnO_2 nanoparticles in comparison with the undoped sample by the decrease in the intensity of SnO_2 peaks when the Eu^{3+} content increased from 0.0 to 10.0%. Because of the interference of Eu^{3+} with SnO_2 lattice, the crystallinity of the Eu^{3+}-doped SnO_2 nanoparticles was worse than that of pure SnO_2. This implies that a portion of Eu^{3+} formed stable solid solutions with SnO_2, it could occur by substituting tin atoms in the crystal structure and that may cause the introduction of point defects and change in stoichiometry due to charge imbalance. The effect leads to a distortion of the crystal structure of the host compound. The crystalline grain sizes of Eu^{3+}-doped SnO_2 nanoparticles decreased from 18.8 to 3.6 nm when the CTAB content increased from 0.0 to 12.5%. The surfactant not only provides a favorable site for the growth of the particulate assemblies, it also influences the formation process, including nucleation, growth, coagulation and flocculation [26,32,33]. It is clear that surfactant CTAB plays a role in the prevention of the growth of crystalline grains of Eu^{3+}-doped SnO_2 nanoparticles.

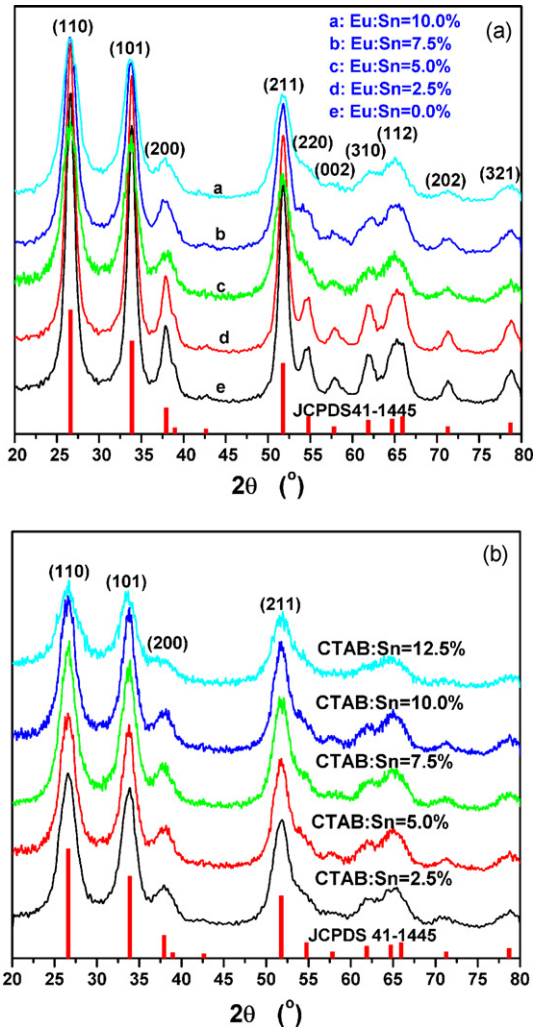

Fig. 2. XRD patters of the samples with different molar ratios Eu^{3+} at CTAB:Sn = 10% (a), and the samples with different molar ratios CTAB at Eu:Sn = 5.0% (b).

The assignment is further confirmed by the refinement of the diffraction patterns with the Rietveld method [34] using the program FULLPROF [35]. For the samples with the different molar ratios Eu^{3+} of 2.5 and 7.5%, the structural parameters calculated from the Rietveld profile refinement are presented in Table 1. The difference curves (Fig. 3) show that the calculated and experimental XRD patterns are in satisfactory agreement, although the significant line broadening due to the small crystallite sizes and microstrain brought in by the heterosubstitution influenced the final agreement between experimental and calculated patterns.

The TEM images of Eu^{3+}-doped SnO_2 nanoparticles prepared under the different Eu^{3+} and CTAB contents are shown in Fig. 4. It could be seen that all SnO_2 nanoparticles are not larger than 7 nm in diameter. The particle sizes agree with the results calculated from XRD patterns. Fig. 4 insets display the corresponding selected-area electron diffraction (SAED) patterns of an ensemble of particles. The spotted diffraction rings from inside to outside can be indexed to the (1 1 0), (1 0 1), (2 0 0), (2 1 1), and (3 0 1) planes of rutile SnO_2, respectively. These indexed patterns are in good accordance with the XRD reflections described above. Moreover, there are no extra polycrystalline rings from Eu or europium oxides. Thus, the Eu^{3+} ions are believed to be dissolved in the SnO_2 structure.

The composition of the Eu^{3+}-doped SnO_2 nanoparticles was further analyzed by XPS. Apart from the C1s peak positioned at 284.0 eV, which originated from spurious amounts of surface

Table 1
Structural data and refinement parameters for Eu^{3+}:SnO_2 nanoparticles (with 2.5 and 7.5% molar ratio) calculated by Rietveld refinement of the experimental XRD powder pattern.

Lattice parameters	Eu:Sn = 2.5%	Eu:Sn = 7.5%
a (Å)	4.739(2)	4.739(2)
c (Å)	3.191(1)	3.196(1)
Unit cell volume (Å^3)	71.672(6)	71.787(6)
Sn/Eu		
x	0	0
y	0	0
z	0	0
O		
x	0.303(4)	0.307(4)
y	0.303(4)	0.307(4)
z	0	0
Average apparent size (nm)	4.1	3.4
Average maximum strain (10^{-4})	4.2311	4.2311
Discrepancy factor (profile-weighted residual error) (R_{WP} (%))	17.7	19.2
Bragg discrepancy factor (R_B (%))	3.64	3.58
Goodness-of-fit indicator (GoF-index)	2.3	2.3

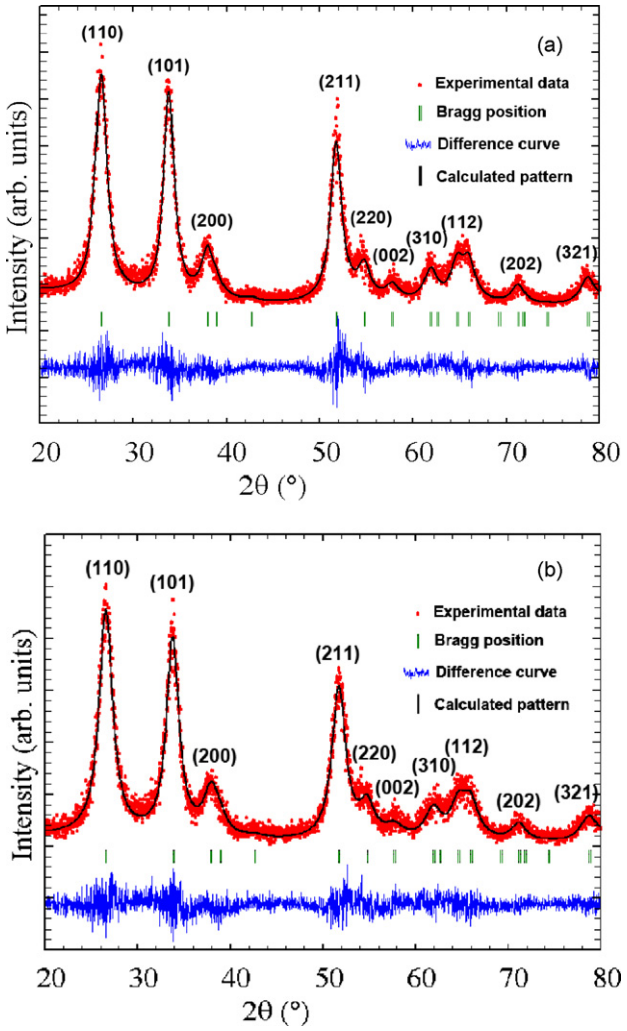

Fig. 3. X-ray diffraction analysis of Eu^{3+}-doped SnO_2 nanoparticles with Eu^{3+} molar ratios at 2.5% (a) and 7.5% (b). The experimental data is shown in red, the calculated patterns in black, and the difference curves in blue. The short vertical bars in green represent the positions of the Bragg reflections. (For interpretation of the references to color in this figure legend, the reader is referred to the web version of the article.)

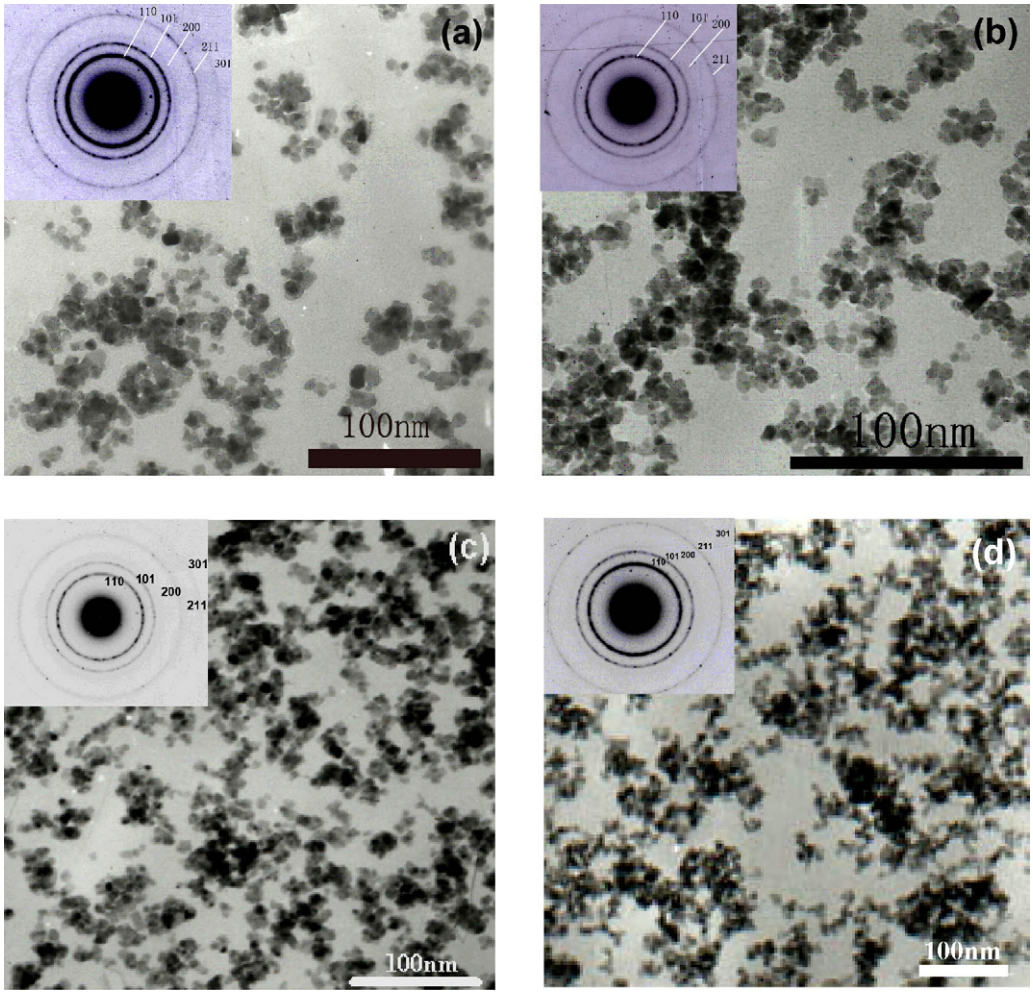

Fig. 4. TEM micrographs of the Eu^{3+}-doped SnO_2 nanoparticles with the different Eu^{3+} and CTAB contents: (a) Eu^{3+}:Sn = 2.5% and CTAB:Sn = 10%; (b) Eu^{3+}:Sn = 5.0% and CTAB:Sn = 10%; (c) Eu^{3+}:Sn = 5.0% and CTAB:Sn = 5.0%; (d) Eu^{3+}:Sn = 5.0% and CTAB:Sn = 12.5%. Insets are selected-area electron diffraction.

carbon of the decomposed CTAB adsorbed onto the inorganic framework of Eu^{3+}-doped SnO_2 nanoparticles, XPS spectra (no shown data) confirmed the high chemical purity of the Eu^{3+}-doped SnO_2 nanoparticles, consisting solely of Sn, Eu and O. Fig. 5(a) shows the high-resolution XPS spectra of the Eu^{3+}-doped SnO_2 nanoparticles with 5.0% molar ratio Eu^{3+}, revealing two peaks of $Sn3d_{5/2}$ and $Sn3d_{3/2}$ at 486.7 and 495.3 eV with a better symmetry, and they were assigned to the lattice tin in SnO_2. The distance between these two peaks was 8.6 eV, being in good agreement with the energy splitting reported for SnO_2. The values correspond to the 3d binding energy of Sn(IV) ions (indexed Standard ESCA Spectra of the Elements and Line Energy Information, *Φ* Co., USA). The corresponding $Eu3d_{5/2}$ spectrum was assigned to binding energy 1135.9 eV (Fig. 5(b)). The evaluation of the areas of the $Sn3d_{5/2}$ and $Eu3d_{5/2}$ emission lines using suitable sensitivity factors (4.89 for $Sn3d_{5/2}$ and 5.0 for $Eu3d_{5/2}$) resulted in an atomic Eu-to-Sn ratio of 4.45%, which is only slightly smaller as compared to the starting recipe. Fig. 5(c) shows that the O1s XPS is asymmetric (the left-hand side is wider), indicating that there are at least two kinds of oxygen species in the near surface region. The peak at about 530.4 eV is due to the SnO_2 crystal lattice oxygen, while that at about 532.4 eV is due to chemisorbed oxygen [36].

The Eu^{3+}-doped SnO_2 nanoparticles display interesting optical properties. UV/Vis spectroscopy was used to characterize the optical absorbance of the Eu^{3+}:SnO_2 nanoparticles. The absorption spectra of Eu^{3+}-doped SnO_2 nanoparticles were carried out to resolve the excitonic or interband (valence-conduction band) transition of Eu^{3+}-doped SnO_2 nanoparticles, which allows us to calculate the bandgap. The UV/Vis absorption spectra of Eu^{3+}:SnO_2 nanoparticles show a strong band edge absorption in the region under 250 nm (Fig. 6). The absorption edge of Eu^{3+}-doped SnO_2 nanoparticles is largely blue-shifted from the absorption edge of SnO_2 bulk. The absorption and corresponding band gap energy of SnO_2 bulk are $\lambda = 350$ nm and $E_g = 3.6$ eV. It is well known that the absorption coefficient of an amorphous semiconductor has a characteristic relation [37]:

$$(\alpha h\nu)^{1/2} = B(h\nu - E_g)$$

in which $h\omega$ is the photon energy, E_g is the apparent optical band gap, B is a constant characteristic of the semiconductor, and α is the absorption coefficient. Therefore, the E_g of the resulted Eu^{3+}-doped SnO_2 nanoparticles can be obtained by the extrapolation of the above relation to be 3.72–3.80 eV (see Fig. 6 inset).

It was reported recently that SnO_2 nanocrystalline thin film has only a broad dominant photoemission peak at 3.13 eV at 300 K [38,39]. For the SnO_2 nanoribbons, there are two strong peaks at 392 nm (3.2 eV) and 439 nm and two weak peaks at 489 and 496 nm at the room temperature [40]. The photoluminescence was attributed to the donor–acceptor pair transitions or to the luminescent center, such as nanocrystals and defects caused by impurities during the growth, but that is not yet clear [38–40]. In our investi-

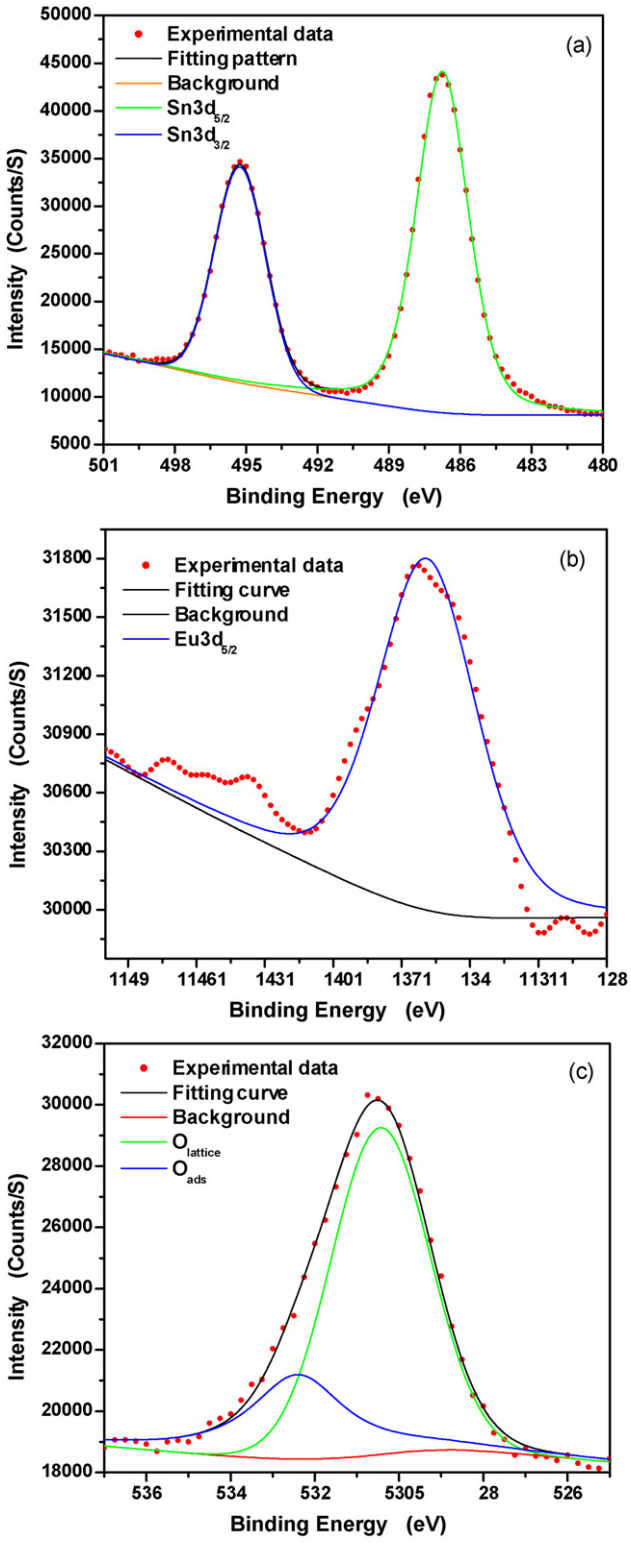

Fig. 5. XPS spectra of Eu^{3+}-doped SnO_2 nanoparticles with 5.0% molar ratio Eu^{3+}: (a) Sn3d, (b) $Eu3d_{5/2}$, and (c) O1s.

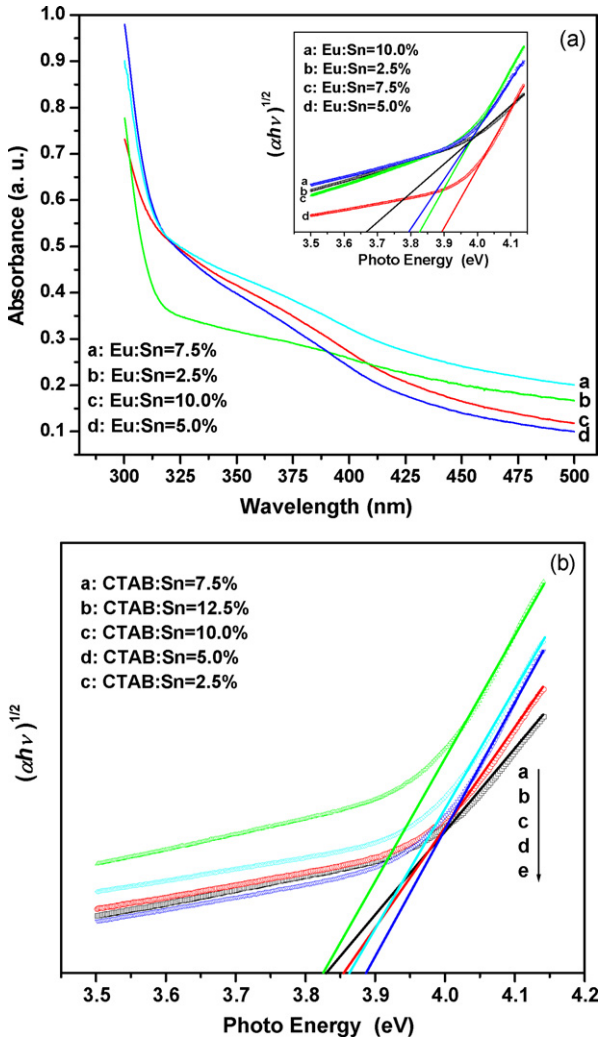

Fig. 6. Absorption spectra of Eu^{3+}-doped SnO_2 nanoparticles with different molar ratios Eu^{3+} (a) and CTAB (b). Inset: apparent energy gap of Eu^{3+}:SnO_2 nanoparticles from the extrapolation of Urbach's equation.

gation, room temperature photoluminescence (RTPL) spectra were performed with the excitation wavelength λ_{ex} = 395 nm and the results are shown in Fig. 7. In the Eu^{3+} fluorescence, the excitation using 394 nm is direct excitation [11]. Fig. 7(a) shows the PL spectra of the Eu^{3+}:SnO_2 nanoparticles with various contents of Eu^{3+} ranging from 0.0 to 10 mol%. The PL intensity reaches the maximum at 5.0% Eu^{3+} and then decreases with further increase of the Eu^{3+} ions content. The two strong lines at 590 and 615 nm are attributed, respectively, to the $^5D_0$–$^7F_1$ magnetic-dipolar transition and $^5D_0$–$^7F_2$ electric-dipolar transition of the Eu^{3+} ions [18]. It was known that only magnetic-dipolar transitions could occur if Eu^{3+} is centrosymmetric in the lattice. Without this inversion symmetry, the electric-dipolar transitions are no longer strictly forbidden and appear in the luminescence spectra [41]. The $^5D_0$–$^7F_2$ band at 615 nm is sensitive to chemical bonds in the vicinity of the Eu^{3+} ion, while the $^5D_0$–$^7F_1$ transition band at 590 nm hardly varies with the crystal field strength around the Eu^{3+} ion. Therefore, the $^5D_0$–$^7F_2$ and $^5D_0$–$^7F_1$ emission intensity ratio indicates the distortion degree of the local environment of the Eu^{3+} ions in the matrix, i.e., the higher the ratio, the lower the site symmetry [42]. From Fig. 7(a), the calculated asymmetry ratios $I(^5D_0$–$^7F_2)/I(^5D_0$–$^7F_1)$ are 1.44, 1.38, 1.11, and 0.95 for the samples with the different molar ratios Eu^{3+} (10.0, 5.0, 7.5, and 2.5%), respectively. It reveals that the Eu^{3+} ion occupies low symmetry sites [11]. The samples with the contents of Eu^{3+} ion of 10.0, 7.5, and 2.5 mol% show an 13, 63, and 75% decrease of the $^5D_0$–$^7F_2$ integrated intensity, respectively. Here, the PL intensity is about 4.0 times higher in the 5.0 mol% content than the intensity in the 2.5 mol% content sample. The PL spectra show a reddish orange emission, and gradually increased with the contents of Eu ions.

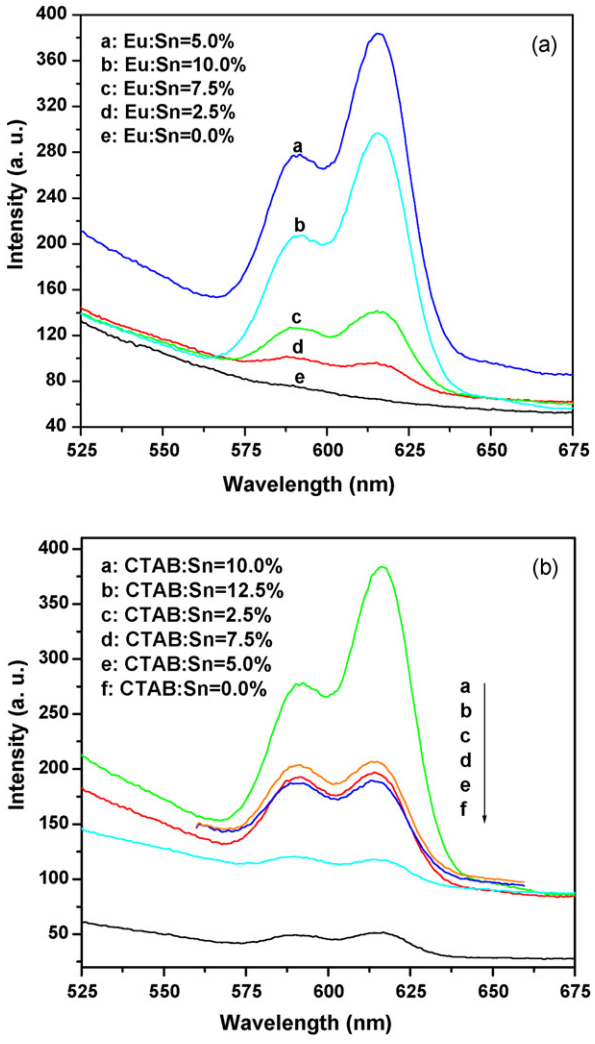

Fig. 7. Emission (λ_{ex} = 395 nm) spectra of Eu^{3+}-doped SnO_2 nanoparticles with different molar ratios Eu^{3+} (a) and CTAB (b).

It is well known that the Sn^{4+} ions in the SnO_2 crystal have a D_{4h} symmetry. If the Eu^{3+} ions correspond to the substitution of Eu^{3+} to the Sn^{4+} ions in the sites of SnO_2, the Eu^{3+} ions should have the same symmetry to that of the Sn^{4+} ions [12]. Fig. 7(b) clearly shows that the emissions intensity changes with increasing the content of surfactant CTAB at 5.0 mol% Eu^{3+}-doped SnO_2 samples. In the present study, we have seen that the PL intensity changes with the variational content of surfactant CTAB, which is a new and interesting result in Eu^{3+}:SnO_2 nanoparticles. In the calcination of as-prepared materials, a lot of the structural defect can be formed because of the decomposition and the removal of the surfactant template. The structural defect has an important influence on photoemission. The maximum PL intensity was observed at 10.0% CTAB, which reveals that structural defect has a profound effect on the emission intensity of the Eu^{3+}:SnO_2 nanoparticles. However, the PL intensity decreases at the 12.5% CTAB content. Our further work is being done to get a definite understanding. In Fig. 7(b), the calculated asymmetry ratios are 1.01, 0.99, 1.01, 1.01, and 0.98% for the samples with the different molar ratios CTAB (12.5, 7.5, 5.0, 2.5, and 0.0%), respectively. It is interesting to note that the symmetry of the substitutional octahedral site is not significantly distorted at various CTAB contents (except the molar ratios CTAB of 10.0%). It reveals that the Eu^{3+} ions occupy the sites of Sn^{4+} ions in the SnO_2 crystal.

4. Conclusions

In summary, Eu^{3+}:SnO_2 nanoparticles with various contents of Eu^{3+} and CTAB ranging from 0.0 to 12.5% were successfully synthesized by a chemical coprecipitation process with the assistance of CTAB. X-ray diffraction, transmission electron micrographs, and photoluminescence are well correlated with the structural characteristics of the Eu^{3+}-doped SnO_2 nanoparticles. The emission intensity of the peak at 614 nm ($^5D_0$–$^7F_2$) for PL exhibits two bands at 590 and 615 nm, respectively. On the basis of a careful investigation of the structure, this study discussed the effect of Eu^{3+} ions and CTAB concentration on the photoluminescence of SnO_2 nanoparticles. It was found that PL properties of Eu^{3+}:SnO_2 nanoparticles are sensitive to the contents of the Eu^{3+} ions and surfactant CTAB.

Acknowledgements

This work was supported by National Natural Science Foundation of China (No. 50662006), and Natural Science Foundation of Yunnan Province, China (No. 2006E0013M).

References

[1] C. Nayarl, T. Ould-Ely, A. Maisonnat, B. Chaudret, P. Fau, L. Lescouzeres, A. Peyre-Lavigne, Adv. Mater. 11 (1999) 61–63.
[2] E.R. Leite, I.T. Weber, E. Longo, J.A. Varela, Adv. Mater. 12 (2000) 965–968.
[3] F.L. Chen, M.L. Liu, Chem. Commun. (1999) 1829–1831.
[4] A.P. Alivisatos, Science 271 (1996) 933–937.
[5] D.J. Norris, A.L. Efros, S.C. Erwin, Science 319 (2008) 1776–1779.
[6] S.C. Erwin, L. Zu, M.I. Haftel, A.L. Efros, T.A. Kennedy, D.J. Norris, Nature 43 (2005) 91–94.
[7] W. Chen, O.J. Malm, V. Zwiller, Y. Huang, S. Liu, R. Wallenberg, O.J. Bovin, L. Samuelson, Phys. Rev. B 61 (2000) 11021–11024.
[8] M. Pal, J.G. Serrano, P. Santiago, U. Pal, J. Phys. Chem. C 111 (2007) 96–102.
[9] K. Biswas, B. Das, C.N.R. Rao, J. Phys. Chem. C 112 (2008) 2404–2411.
[10] K. Ebisawa, T. Okuno, K. Abe, Jpn. J. Appl. Phys. 47 (2008) 72367–73238.
[11] A. Kar, A. Patra, J. Phys. Chem. C 113 (2009) 4375–4380.
[12] M. Nogami, A. Ohno, H. You, Phys. Rev. B 68 (2003) 104204–104210.
[13] M. Nogami, T. Enomot, T. Hayakawa, J. Lumin. 97 (2002) 147–152.
[14] T. Moon, S.T. Hwang, D.R. Jung, D. Son, C. Kim, J. Kim, M. Kang, B. Park, J. Phys. Chem. C 111 (2007) 4164–4167.
[15] F. Gu, S.F. Wang, M.K. Lü, Y.X. Qi, G.J. Zhou, D. Xu, D.R. Yuan, Opt. Mater. 25 (2004) 59–64.
[16] P.S. Chowdhury, S. Saha, A. Patra, Solid State Commun. 131 (2004) 785–788.
[17] X.Y. Fu, H.W. Zhang, S.Y. Niu, Q. Xin, J. Solid State Chem. 178 (2005) 603–607.
[18] A.C. Yanes, J.D. Castillo, M. Torres, J. Peraza, V.D. Rodríguez, J. Méndez-Ramos, Appl. Phys. Lett. 85 (2004) 2343–2345.
[19] B.L. Cushing, V.L. Kolesnichenko, C.J. O'Connor, Chem. Rev. 104 (2004) 3893–3946.
[20] V. Dusastre, D.E. Williams, J. Phys. Chem. B 102 (1998) 6732–6737.
[21] R. Koivula, R. Harjula, J. Lehto, Micropor. Mesopor. Mater. 55 (2002) 231–238.
[22] L.L. Li, L.M. Mao, X.C. Duan, Mater. Res. Bull. 41 (2006) 541–546.
[23] W. Posthumus, J. Laven, G. de With, R. van der Linde, J. Colloid Interf. Sci. 304 (2006) 394–401.
[24] J.R. Zhang, L. Gao, Mater. Res. Bull. 39 (2004) 2249–2255.
[25] J.R. Zhang, L. Gao, Inorg. Chem. Commun. 7 (2004) 91–93.
[26] S.G. Dixit, A.R. Mahadeshwar, S.K. Haram, Colloids Surf. A: Physicochem. Eng. Aspects 133 (1998) 69–75.
[27] I. Djerdj, D. Arcon, Z. Jaglicic, M. Niederberger, J. Phys. Chem. C 111 (2007) 3614–3623.
[28] I. Djerdj, A.M. Tonejc, J. Alloys Compd. 413 (2006) 159–174.
[29] J.S. Beck, J.C. Vartuli, W.U. Roth, M.E. Leonowicz, C.T. Kresge, K.D. Schmitt, C.T.W. Chu, D.H. Olson, E.W. Sheppard, S.B. McCullen, J.B. Higgins, J.L. Schlenker, J. Am. Chem. Soc. 114 (1992) 10834–10843.
[30] A. Sayari, I.L. Moudrakovski, J.S. Reddy, C.I. Ratcliffe, J.A. Ripmeester, K.F. Preston, Chem. Mater. 8 (1996) 2080–2088.
[31] Q. Gao, J. Chen, R. Xu, Y. Yue, Chem. Mater. 9 (1997) 457–462.
[32] Y.D. Wang, C.L. Ma, X.D. Sun, H.D. Li, Nanotechnology 13 (2002) 565–569.
[33] Y.D. Wang, C.L. Ma, X.D. Sun, H.D. Li, Inorg. Chem. Commun. 5 (2002) 751–755.
[34] L.B. McCusker, R.B. Von Dreele, D.E. Cox, D. Louer, P. Scardi, J. Appl. Crystallogr. 32 (1999) 36–50.
[35] J. Rodriguez-Carvajal, FullProf, version 1.9c, LLB, CEA/Saclay, France, 2001.
[36] M. Koudelka, A. Monnier, J. Sanchez, J. Augustynski, J. Mol. Catal. 25 (1984) 295–305.

[37] G. Mill, Z.G. Li, D. Meisel, J. Phys. Chem. 92 (1988) 822–828.
[38] T.W. Kim, D.U. Lee, J.H. Lee, D.C. Choo, M. Jung, Y.S. Yoon, J. Appl. Phys. 90 (2001) 175–180.
[39] T.W. Kim, D.U. Lee, Y.S. Yoon, J. Appl. Phys. 88 (2000) 3759–3761.
[40] J.Q. Hu, X.L. Ma, N.G. Shang, Z.Y. Xie, N.B. Wong, C.S. Lee, S.T. Lee, J. Phys. Chem. B 106 (2001) 3823–3826.
[41] G. Blasse, B.C. Grabmaier, Luminescent Materials, Springer-Verlag, New York, 1994.
[42] S.N.B. Bhaktha, F. Beclin, M. Bouazaoui, B. Capoen, A. Chiasera, M. Ferrari, C. Kinowski, G.C. Righini, O. Robbe, S. Turrell, Appl. Phys. Lett. 93 (2008) 2119041–2119043.